Seasonal and hemispheric asymmetries in the cold ion outflow source region: Swarm and CHAMP observations of F-region polar cap plasma density

S. M. Hatch[1*], S. Haaland[1,2], K. M. Laundal[1], T. Moretto[1], A. W. Yau[3], L. Bjoland[4], J. P. Reistad[1], A. Ohma[1], K. Oksavik[1,4]

[1]Birkeland Centre for Space Science, University of Bergen, Norway
[2]Max-Planck Institute for Solar Systems Research, Göttingen, Germany
[3]Department of Physics and Astronomy, University of Calgary, Calgary, Alberta, Canada
[4]Department of Arctic Geophysics, University Centre in Svalbard, Longyearbyen, Norway

Key Points:

- Statistics of F-region polar cap plasma density derived from 15 years of measurements exhibit several types of seasonal asymmetries
- Southern Hemisphere polar cap plasma densities lag those in Northern Hemisphere by at least two weeks around local spring and fall equinox
- Hemispheric differences in polar cap plasma density at equinoxes cannot be explained solely on the basis of differences in illumination

*Department of Physics and Technology, Allégaten 55, N-5007 Bergen, Norway

Corresponding author: S. M. Hatch, Spencer.Hatch@uib.no

Abstract

One of the primary mechanisms of loss of Earth's atmosphere is the persistent "cold" ($T \lesssim 20$ eV) ion outflow that has been observed in the magnetospheric lobes over large volumes with dimensions of order several Earth radii (R_E). As the main source of this cold ion outflow, the polar cap F-region ionosphere and conditions within it have a disproportionate influence on these magnetospheric regions. Using 15 years of measurements of plasma density N_e made by the Swarm spacecraft constellation and the CHAMP spacecraft within the F region of the polar cap above 80° Apex magnetic latitude, we report evidence of several types of seasonal asymmetries in polar cap N_e. Among these, we find that the transition between "winter-like" and "summer-like" polar cap N_e occurs one week prior to local spring equinox in the Northern Hemisphere (NH), and one week after local spring equinox in the Southern Hemisphere (SH). Thus SH polar cap N_e lags NH polar cap N_e by approximately two weeks with respect to local spring and fall equinox in each hemisphere. We show that this lag cannot be explained by differences in solar illumination alone. We also find that overall variation of N_e in the SH polar cap is greater than overall variation of N_e in the NH polar cap, except for an approximately two-month period centered on June solstice, and that the greater degree of variability of N_e in the SH polar cap is partly attributable to differences in illumination of the SH polar cap.

Plain Language Summary

The Earth's magnetic poles are not perfectly aligned with the Earth's geographic poles, and the degree of misalignment is greater in the Southern Hemisphere. Furthermore, as a result of the Earth's elliptical orbit around the Sun, summer and fall in the Northern Hemisphere together are approximately one week longer than summer and fall in the Southern Hemisphere, and the Earth is very slightly closer to the Sun around December solstice (summer in the Southern Hemisphere). These seasonal asymmetries, together with the asymmetric displacement of the Earth's magnetic poles relative to the geographic poles, suggest that the plasma density in the topside ionosphere's geomagnetic polar regions may also be subject to seasonal and hemispheric asymmetries. The polar regions are the primary site of loss of the Earth's atmosphere via so-called ion outflow processes that over geological time scales are believed to lead to a non-negligible loss of the Earth's atmosphere. Using 15 years of plasma density measurements made by four different satellites to statistically study the plasma density of each hemisphere's geomag-

netic polar cap ionosphere in the altitude range 350–520 km, we find that the polar cap ionosphere at these altitudes exhibits a variety of seasonal and hemispheric asymmetries.

1 Introduction

A substantial fraction of the plasma in the Earth's magnetosphere is supplied by the ionosphere (e.g., Chappell et al., 1987, 2000) through ion outflow from the high-latitude polar cap regions, where terrestrial magnetic field lines are open and connected to solar wind magnetic field lines. By the same token, ion outflow is also considered to be a primary means of loss of the Earth's atmosphere (e.g., André, 2015). Ion outflow is the result of ionization of atmospheric gases and outward transport due to vertical forces. Recent results suggest that low-energy ions from the open polar cap area usually dominate the ion density and the outward flux in populating large volumes of the magnetosphere. Furthermore, ionization (i.e., availability of free charges) rather than transport is reported to be the limiting factor for ion outflow (Haaland et al., 2012; André et al., 2015).

Ionization is primarily driven by solar illumination, although other processes such as cosmic rays (e.g., Adams & Masley, 1965; Velinov, 1970) and particle precipitation also contribute (e.g., Rees, 1963, 1982). Solar radiation at ultraviolet (UV) and extreme ultraviolet (EUV) wavelengths is the most efficient in terms of ionizing atmospheric atoms and molecules and producing ion-electron pairs (e.g., S. E. Appleton, 1956; Ivanov-Kholodnyy, 1962; Rees, 1989; Brekke, 1997; Schunk & Nagy, 2009). Since the ionosphere as a whole is quasi-neutral, both the electron number density and ion number density are often simply referred to as the plasma density.

The resulting plasma density in the atmosphere is a balance between production (ionization) processes on one hand, and losses by recombination and transport processes on the other hand (e.g., Quinn & Nisbet, 1965; Khocholava, 1977; Rees, 1989; Rishbeth, 1997). Production and loss processes do not necessarily work on the same time scale, so at a given location in space, there can be significant variation in the plasma density over time.

In the terrestrial atmosphere, the peak plasma density is typically located in the ionospheric F-layers, around 200–400-km geodetic altitude (e.g., Rishbeth, 1962; Feldstein et al., 1975). Since ionization is strongly driven by solar illumination, plasma den-

sity exhibits solar cycle variations as well as strong seasonal and diurnal variations (e.g., E. V. Appleton, 1939). Typical plasma densities are of order 10^5–10^6 cm^{-3} in the sunlit ionosphere, but can be less by an order of magnitude or two in darkness.

In the polar regions the variation of plasma density with season is strongest, followed by diurnal variation and variation with solar cycle (e.g., Feldstein et al., 1975). The seasonal variation can largely be understood on the basis of solar illumination; during summer conditions, the polar cap is fully illuminated. Conversely, during winter conditions major portions of the polar cap are in complete darkness. The Sun-Earth distance plays a lesser, though non-negligible, role for variations in solar illumination (e.g., Dang et al., 2017). From the standpoint of plasma density variation, one would expect solar illumination, ionization and plasma production to be very similar in the Northern and Southern Hemisphere around equinox.

In contrast to ionization and production of ionospheric plasma, which are primarily due to solar EUV radiation, transport of ionospheric plasma is primarily driven by electromagnetic forces and organized with respect to the geomagnetic rather than the geographic poles. Horizontal transport is mainly driven by large scale magnetospheric convection set up by reconnection at the dayside magnetopause (e.g., Dungey, 1963), and thermospheric neutral winds (e.g., Förster et al., 2008). Vertical transport—upflow and outflow—is due to a combination of various forces. Theoretical descriptions of ion outflow at the polar caps were developed in the 1960s (e.g. Dessler & Michel, 1966; Nishida, 1966; Axford, 1968; Banks & Holzer, 1968) and collectively comprise the classical polar wind paradigm. In this view, light ion species in the ionosphere gain upward mobility via plasma and neutral pressure gradients as well as ambipolar electric fields formed and sustained by requiring charge balance between electrons and ions in the ionosphere. Due to the mirror force, any additional transverse acceleration near and above the exobase (500–1000 km) effectively acts as upward acceleration (e.g., Klumpar, 1979). At altitudes of a few R_E, centrifugal forces (Cladis, 1986; Horwitz et al., 1994; C. Liu et al., 1994; Nilsson et al., 2008, 2010) become dominant.

Thus, the significant difference in magnetic topology of the Northern and Southern Hemisphere polar regions (e.g., Cnossen & Förster, 2016; K. Laundal et al., 2017) is a likely factor in reported hemispheric asymmetries in ionospheric outflow around equinox (e.g., Maes et al., 2016; Haaland et al., 2017; Li et al., 2020). These differences do play

a role, for example, in the seasonal variation of thermospheric and ionospheric winds (Aruliah, Farmer, Fuller-Rowell, et al., 1996; Aruliah, Farmer, Rees, & Brändström, 1996; Mikhailov & Schlegel, 2001).

Estimation of the total loss of geogenic plasma due to ion outflow is subject to additional complications that arise because the source regions (primarily the open polar cap, but also cusp and auroral zone) vary greatly in size and shape in response to solar wind driving (Sotirelis et al., 1998; Milan et al., 2008; Milan, 2009; Li et al., 2012).

In this study, we follow up on previous studies (Haaland et al., 2012; André et al., 2015; Haaland et al., 2017) indicating or otherwise suggesting that available ionospheric plasma rather than transport is the limiting factor for ion outflow. Using a large database of ionospheric plasma density measurements made by the Swarm and CHAMP satellites in both hemispheres, we seek to determine under which seasons hemispheric asymmetries in cold plasma outflow might be expected on the basis of available ionospheric plasma.

This study is organized as follows. In section 2 we describe the Swarm and CHAMP polar cap plasma density database. In section 3 we identify and describe a number of seasonal and hemispheric asymmetries in polar cap plasma density. In section 4 we consider differences in illumination and plasma production of the two polar caps using a simple model. In section 5 we discuss results from the preceding section and describe some implications for cold ion outflow. In section 6 we summarize the results of this study and conclude. We additionally describe in Appendix A–B various methodological details of this study.

2 Swarm and CHAMP Plasma Density Measurements

We use plasma density measurements made by two separate missions, the original three-satellite Swarm constellation (Friis-Christensen et al., 2008) and the Challenging Mini-Satellite Payload (CHAMP) satellite (Reigber et al., 2006).

The original three Swarm satellites complete approximately 15 orbits per day in a near-polar orbit, over the six-year period extending from launch on 22 November 2013 to the present. The two lower satellites, Swarm Alpha (Swarm A) and Swarm Charlie (Swarm C), cover the range of geodetic altitudes between 445 km and 500 km (up to 527 km during commissioning phase); Swarm Bravo (Swarm B) covers the range of geodetic altitudes between 510–545 km (down to 500 km during commissioning phase). The

Electric Field Instrument (EFI) (Knudsen et al., 2017) aboard the three original Swarm satellites includes two dedicated low-gain and high-gain Langmuir Probes (LPs). The two LPs measure plasma density and electron temperature at 2 Hz. The most complete in-flight calibrations and validations of the Swarm LP plasma density and electron temperature measurements, based on comparisons with plasma density measurements measured by other satellites and ground-based instruments, have been performed by Lomidze et al. (2018).

The CHAMP satellite also completed approximately 15 orbits per day in a near-polar orbit over a ∼10-year period extending from 15 July 2000 to 19 September 2010. The nominal range of geodetic altitudes covered by CHAMP extended over ∼300–455 km. The Planar Langmuir Probe (PLP) instrument (Rother et al., 2005) aboard CHAMP made measurements of plasma density at a 15-s cadence. In-flight calibration of the PLP instrument has been performed by McNamara et al. (2007).

In this study we use all Swarm Level 1B LP plasma density measurements downsampled to 15-s cadence, from the period between 10 Dec 2013 to 5 Feb 2020 (`https://swarm-diss.eo.esa.int/`). Downsampling is achieved by selecting every 30th measurement. We also use all CHAMP Level 2 PLP plasma density measurements from the period between 19 Feb 2002 and 21 Dec 2009 (`ftp://isdcftp.gfz-potsdam.de`) made at ≥350-km geodetic altitude. We impose this altitude restriction on CHAMP density measurements to ensure that all plasma density measurements are made above the altitude at which the $F2$-layer plasma density peak $hmF2$ is located (e.g., Shim et al., 2011; Burns et al., 2012; Bjoland et al., 2016). To Swarm plasma density measurements we also apply the Lomidze et al. (2018) in-flight calibrations (see Appendix A). Since ion outflow and ionosphere-magnetosphere coupling are organized by the geomagnetic field we are here concerned with the geomagnetic polar cap, which we define (Table 1) as the region at and above 80° magnetic latitude (MLat) in the Modified Apex coordinate system at a reference geodetic altitude of 110 km (i.e., MA_{110} coordinates) (Richmond, 1995; K. M. Laundal & Richmond, 2016). We perform the conversion of geocentric coordinates of each satellite to MA_{110} coordinates via the `apexpy` Python package (Emmert et al., 2010; van der Meeren et al., 2018). Table 1 summarizes some properties of the polar caps in each coordinate system.

Table 1. Definitions and properties of the geomagnetic and geocentric polar caps.

Hemisphere	Polar cap	Area[a] (km^2)	Circumference[a] (km)
	Geomagnetic (MA_{110}) coordinates		
North	$\geq 80^\circ$ MLat[b]	3.98×10^6	7.11×10^3
South	$\leq -80^\circ$ MLat	3.65×10^6	6.76×10^3
	Geocentric coordinates		
North	$\geq 80^\circ$ Lat[c]	3.91×10^6	6.98×10^3
South	$\leq -80^\circ$ Lat	3.91×10^6	6.98×10^3

[a]Area and perimeter at 0-km altitude.

[b]MLat ≡ Magnetic latitude in MA_{110} coordinates (see text).

[c]Lat ≡ Latitude in geocentric coordinates.

The total number of plasma density (N_e) measurements in the Northern Hemisphere (NH) and Southern Hemisphere (SH) geomagnetic polar caps are respectively 2,410,423 and 1,045,654. The primary reasons for the greater statistical coverage of the NH geomagnetic polar cap are that the SH geomagnetic polar cap area is approximately 9% smaller than the NH geomagnetic polar cap area (Table 1 and Figure S1 in Supporting Information), and that the relative displacement between the SH geomagnetic and geographic poles is greater compared with the NH poles. The difference in geomagnetic polar cap area arises because the Earth's magnetic field is stronger in the vicinity of the SH magnetic pole than in the vicinity of the NH magnetic pole (K. Laundal et al., 2017). The measurement coverage is approximately the same in both hemispheres (2.64 and 2.68 million measurements in the NH and SH geocentric polar caps, respectively) if one instead considers the polar caps defined in a geocentric coordinate system.

In the remainder of the manuscript all references to N_e and statistics refer only to measurements made in the geomagnetic polar caps, unless specified otherwise.

We seek to investigate seasonal and hemispheric asymmetries via statistical comparison of plasma density measurements in the geomagnetic polar cap made by different satellites. Such an investigation is complicated by a number of factors, including:

1. Differences in the altitudes of each satellite, which vary on time scales of days and years due to satellite drag and operational maneuvers, and which are systemat-

193 ically different in the two hemispheres due to both the shape of each satellite's or-
194 bit and the oblateness of the Earth (section A1). These differences correspond to
195 sampling of different heights in the ionosphere.
196 2. Variations in solar and geomagnetic activity, which lead to differences in ionospheric
197 conditions.

198 We partially account for these factors via (i) application of an empirically derived scale
199 height to N_e measurements that "maps" N_e to a common geodetic altitude of 500 km,
200 and (ii) application of an empirically derived correction factor that accounts for the vari-
201 ation of N_e measurements with 10.7-cm wavelength solar radio flux (otherwise known
202 as the $F10.7$ index). The latter correction scales N_e to a nominal solar activity of $\langle F10.7\rangle_{27} =$
203 80, where $\langle F10.7\rangle_{27}$ is a rolling average of the preceding 27 days of the $F10.7$ index. Through-
204 out this manuscript we use the notation N_e^* to refer to these final adjusted densities. De-
205 tailed descriptions of the derivation of the relevant scaling factors are located in Appendix
206 A.

207 3 Hemispheric and Seasonal N_e^* Variations

208 Figure 1a shows height- and solar-flux adjusted plasma density N_e^* in the NH (blue)
209 and SH (red) geomagnetic polar caps as a function of day of year. The transparent "x"
210 and "+" markers respectively indicate 50,000 randomly selected individual measurements
211 made in the NH and SH geomagnetic polar cap for each hemisphere. The solid blue and
212 dashed red lines respectively indicate the median NH and SH N_e^* values within 10-day
213 bins. The error bars indicate the 95% confidence interval of the median, calculated as
214 described in Appendix B.

215 One of the apparent differences between the median N_e^* values in the NH and SH
216 geomagnetic polar cap is that N_e^* takes on more extreme values in the SH than in the
217 NH. This difference may be related to the "ionospheric annual asymmetry," which has
218 to do with global ionospheric plasma densities around December solstice that are larger
219 than global ionospheric plasma densities around June solstice by ∼30%. This effect is
220 well documented but not yet fully understood (e.g. Mendillo et al., 2005; Torr et al., 1980;
221 Rishbeth & Müller-Wodarg, 2006; Lei et al., 2016; Dang et al., 2017; Xiong et al., 2018;
222 Chartier et al., 2019); it may result from a combination of solar irradiance and photo-
223 chemistry effects (Dang et al., 2017). Variation of Sun-Earth distance alone can only ac-

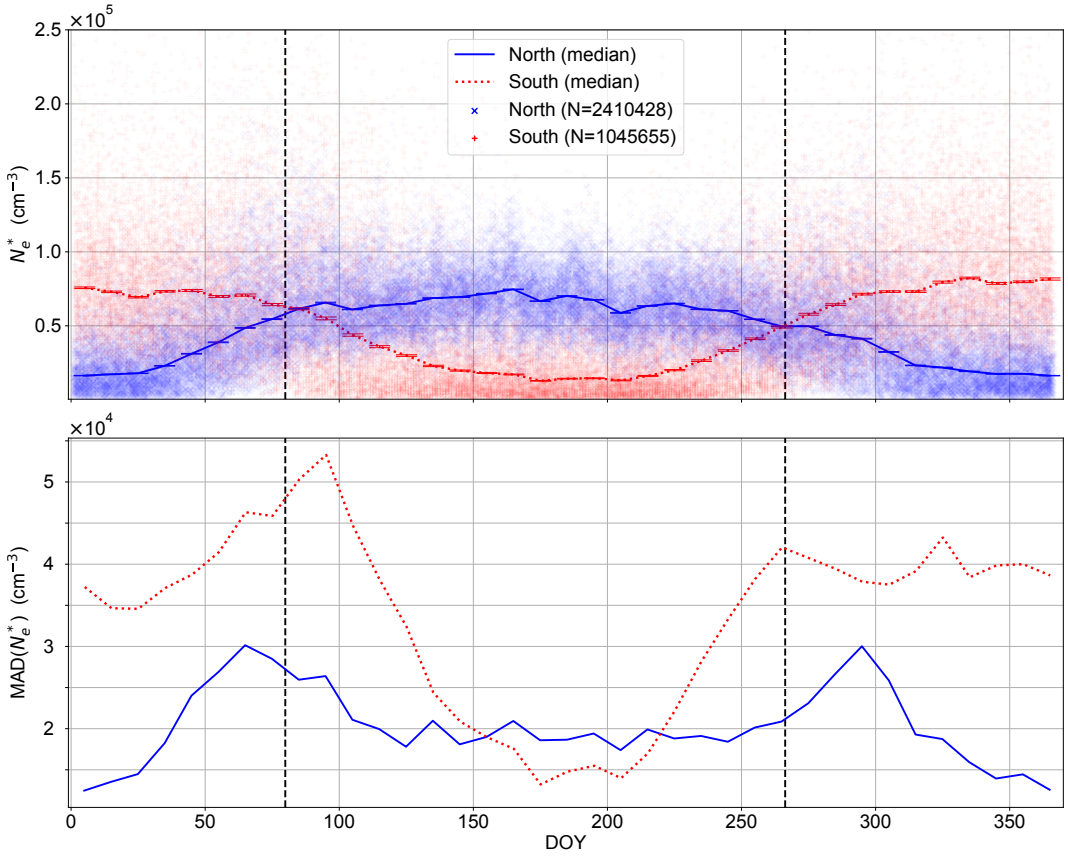

Figure 1. Swarm and CHAMP height- and solar flux-adjusted geomagnetic polar cap plasma density N_e^* statistics versus day of year in the Northern Hemisphere (solid blue line) and Southern Hemisphere (dashed red line). Here N_e^* denotes plasma density measurements that are scaled to a common geodetic altitude of 500 km and to a nominal solar activity of $\langle F10.7 \rangle_{27} = 80$, as described in Appendix A. (a) N_e^* measurements and binned medians. The transparent "x" and "+" markers respectively indicate 50,000 randomly selected individual measurements made in the NH and SH geomagnetic polar cap for each hemisphere. (Most readers will need to view the plot at full resolution or zoom in to see the distinction between these symbols.) Median N_e^* values within each 10-day bin are respectively indicated by the solid blue (North) and dashed red (South) line. Error bars indicate the 95% confidence interval of the bin median, calculated as described in Appendix B. (b) MAD(N_e^*) in the NH (solid blue line) and SH (dashed red line) geomagnetic polar caps, in 10-day bins. In both panels the dotted black lines at DOY $\approx$ 79.9 and DOY $\approx$ 266.3 respectively indicate the average DOY on which March and September equinoxes occur during the years 2000–2020; the time and date of each equinox is calculated as described in section 3. MAD≡median absolute deviation.

count for global differences of 7%, and therefore is alone insufficient to account for the observed asymmetry (Rishbeth & Müller-Wodarg, 2006).

Central tendency and variation of a statistical quantity are often indicated by the mean and standard deviation, respectively. However, N_e^* distributions in each bin in Figure 1a are heavy-tailed, and the mean is not a robust indicator of central tendency. In Figure 1a we therefore show median N_e^* statistics in each bin. Likewise, in Figure 1b we show the median absolute deviation

$$\mathrm{MAD}(N_e^*) \equiv \mathrm{median}\,|N_e^* - \mathrm{median}\,(N_e^*)|$$

instead of standard deviation to indicate the variation of N_e^* in each 10-day bin. Figure 1b shows $\mathrm{MAD}(N_e^*)$ in the Northern and Southern Hemisphere as solid blue and dashed red lines, respectively.

Two salient aspects of $\mathrm{MAD}(N_e^*)$ curves in Figure 1b are (i) the SH $\mathrm{MAD}(N_e^*)$ is typically greater than NH $\mathrm{MAD}(N_e^*)$; (ii) $\mathrm{MAD}(N_e^*)$ in the NH geomagnetic polar cap evinces two distinct peaks, before March equinox and after September equinox, while $\mathrm{MAD}(N_e^*)$ in the SH geomagnetic polar cap evinces one primary peak after March equinox, a $\mathrm{MAD}(N_e^*)$ "plateau" that extends from September to the end of December, and a global minimum near June solstice.

3.1 Asymmetries in seasonal variation

We now compare variations in N_e^* as a function of season. We wish to (i) avoid the systematic bias that would be introduced by performing a comparison based on day of year in the Gregorian calendar, which is inherently asymmetric from year to year with respect to the day of year on which equinoxes and solstices occur; (ii) consistently account for variation in the length of the seasons themselves, which differ on the order of days. To accomplish this, we scale the precise time period between each equinox and solstice for each year such that the period between each equinox and solstice has a duration of 1, and the total duration of all four seasons (i.e., one year) is 4. We thus define the "season parameter" $\phi_s \in [0, 4)$, with March and September equinoxes respectively corresponding to $\phi_s = 0$ and $\phi_s = 2$. June and December solstices respectively correspond to $\phi_s = 1$ and $\phi_s = 3$. The timestamps of all N_e^* measurements are then scaled to values between 0 and 4. The date and time of occurrence of each equinox and solstice

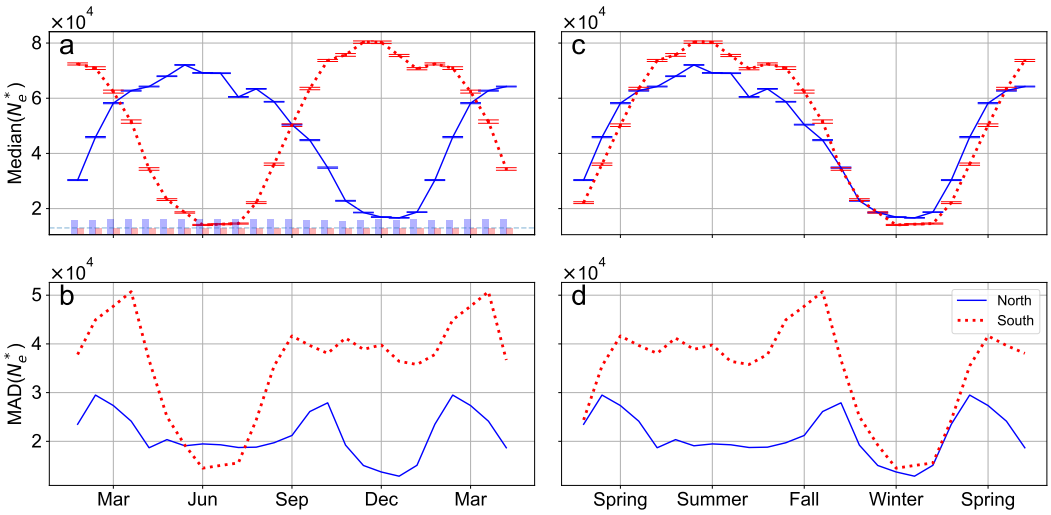

Figure 2. Median and median absolute deviation (MAD) of Swarm and CHAMP height- and solar flux-adjusted geomagnetic polar cap plasma density N_e^* statistics versus season parameter ϕ_s (see section 3.1) in the Northern Hemisphere (solid blue line) and Southern Hemisphere (dotted red line). Tick marks in each panel precisely indicate the relevant equinox or solstice. (a) Median N_e^* in each hemisphere as a function of season. (b) MAD(N_e^*) in each hemisphere as a function of season. (c) Median N_e^* in each hemisphere as a function of local season. (d) MAD(N_e^*) in each hemisphere as a function of local season. Error bars in Figures 2a and 2c indicate the 95% confidence interval of the median, calculated as described in Appendix B. The transparent histograms at the bottom of Figure 2a indicate the number of N_e^* values used to calculate the median statistic in each bin. The average number of measurements in each bin is $120,000$ in the NH and $52,500$ in the SH; the dashed gray line indicates $N = 54,000$. The total number of SH measurements is about 60% less than the total number of NH measurements (see section 2).

for all relevant years between 2002 and 2020 is calculated to second precision via the `skyfield` Python package (Rhodes, 2019).

Figure 2a displays median N_e^* values in the NH (solid blue line) and SH (dotted red line) geomagnetic polar caps as a function of the season parameter ϕ_s for bins of 0.2. The error bars indicate the 95% confidence interval of the median in each bin, calculated via the methodology described in Appendix B. At March equinox the median value of SH N_e^* is $7 \pm 1\%$ greater than the value of NH N_e^*, while there is apparently no such asymmetry ($0.4 \pm 1\%$) around September equinox.

Figure 2b displays MAD(N_e^*) in each hemisphere. In addition to the general trends in MAD(N_e^*) described at the beginning of this section, here it is also apparent that the combined hemispheric MAD(N_e^*) at December solstice are greater than the combined hemispheric MAD(N_e^*) around June solstice. The globally greater variability of F-region N_e^* around December solstice has been shown (Chartier et al., 2019) to result from a combination of the ionospheric annual asymmetry and O^+ plasma lifetimes that are longer during December solstice than during June solstice.

Figure 2c displays median N_e^* values in the NH (solid blue line) and SH (dotted red line) geomagnetic polar caps as a function of local season ϕ_s, where the phase of the SH ϕ_s season parameter values is shifted backward by 2 to facilitate comparison of local seasonal variations in median N_e^* for each hemisphere. From this figure it is immediately apparent that (i) the range of median SH N_e^* values in the SH is overall larger than the range of median NH N_e^* values, which is also visible in Figure 1a, and (ii) variation in median SH N_e^* lags behind median NH N_e^* around local spring and fall equinoxes by several days. We quantify this lag in the following subsection. These statistics also suggest that the annual maximum in median NH N_e^* occurs before local summer solstice, while the annual maximum in median SH N_e^* occurs at or perhaps slightly before local summer solstice. A secondary peak in median N_e^* between local summer solstice and local fall equinox is also apparent in both hemispheres.

Figure 2d displays MAD(N_e^*) in each hemisphere as a function of local season. The most immediate observation is that SH MAD(N_e^*) (dotted red line) are almost always greater than NH MAD(N_e^*) (solid blue line), except for the period between local winter and local spring where the MAD(N_e^*) values in each hemisphere are similar. Beyond this basic difference, in both hemispheres MAD(N_e^*) peaks after local fall, reaches a global minimum near local winter, and either peaks (in the NH) or plateaus (in the SH) near local spring.

3.2 Equinoctial Asymmetries

We now consider the evolution of N_e^* around equinox in each hemisphere. Figure 3a shows median NH N_e^* values relative to March equinox (thin blue line) and September equinox (thick blue line) in 15-day bins. Crossover occurs at -7.2 days relative to equinox. Figure 3b shows median SH N_e^* values relative to March equinox (thin red dotted line)

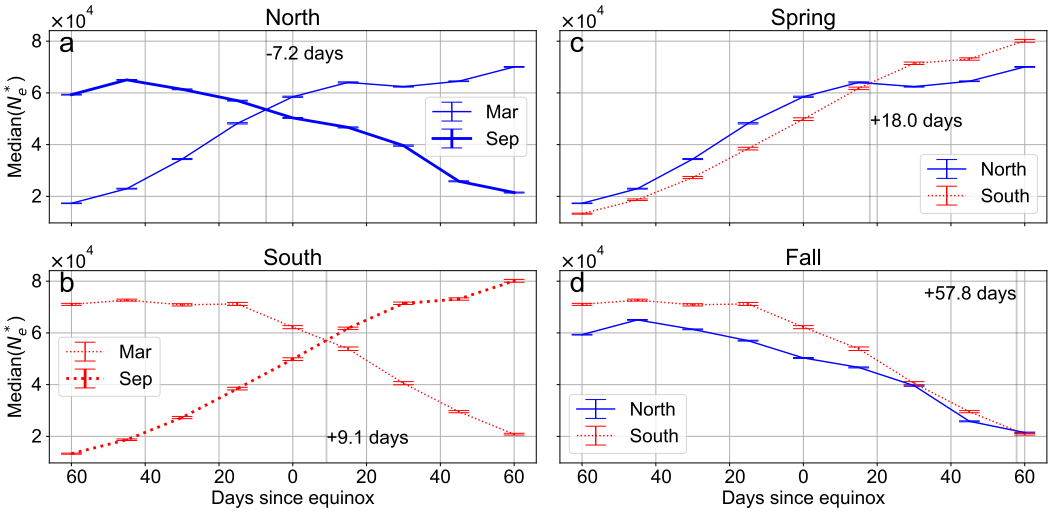

Figure 3. Median N_e^* statistics in 15-day bins relative to the number of days since equinox (Figures 3a–d). (a) Median NH N_e^* relative to March equinox (thin blue line) and September equinox (thick blue line). (b) Median SH N_e^* relative to March equinox (thin dotted red line) and September equinox (thick dotted red line). (c) Median NH N_e^* (solid blue line) and SH N_e^* (dotted red line) relative to local spring equinox. (d) Median NH N_e^* (solid blue line) and SH N_e^* (dotted red line) relative to local fall equinox. The 95% confidence intervals of the medians in 3a–d are calculated as described in Appendix B.

and September equinox (thick dotted red line). Crossover occurs at +9.1 days relative to equinox. Figure 3c shows NH and SH median N_e^* values relative to March and September equinox, respectively, and Figure 3d shows NH and SH median N_e^* values relative to September and March equinox, respectively. That is, Figure 3c and 3d show median N_e^* values in each hemisphere relative to local spring and fall, respectively.

Figure 3c shows that the local spring crossover between median NH N_e^* (solid blue line) and median SH N_e^* (dotted red line) occurs at +18 days relative to equinox. Figure 3d shows that the local fall crossover between median NH N_e^* (solid blue line) and median SH N_e^* (dotted red line) occurs at +58 days relative to equinox, but it is also apparent that these lines are very near one another over approximately +30 to +60 days after equinox. To calculate the crossover point in each panel, we interpolate between each 15-day median with a resolution of 0.1 days and determine the relative day of year for which the two lines shown in each panel are nearest each other.

4 Hemispheric and Seasonal Variations in Solar Illumination

Of the factors that influence the production of ionospheric plasma (see Introduction), solar illumination is perhaps the most important. To determine which, if any, of the asymmetries identified in the previous section can be explained purely on the basis of solar illumination, we have conducted the analysis of geomagnetic and geocentric polar cap illumination shown in Figure 4, with x axes indicating the season or local season as in Figure 2. The top row (Figures 4a–b) shows solar zenith angle χ ranges for the NH (dotted blue line and cross hatching) and SH (dotted red line and circle hatching) geomagnetic polar caps. The fourth row (Figures 4g–h) shows χ ranges for the geocentric polar caps. Gray shading in the upper half of Figures 4a–b and g–h indicates the range $\chi > \chi_m$, where, from basic trigonometry,

$$\chi_m\left(h_0\right) = \frac{\pi}{2} + \arccos\left(\frac{R}{R+h_0}\right) \tag{1}$$

is the maximum solar zenith angle at which the Sun is visible as a function of reference altitude h_0 and Earth radius R =6371 km, neglecting refraction of sunlight and the oblateness of Earth. At reference altitude h_0 =350 km, $\chi_m \approx 108.6°$.

The range of χ values for each day is produced by identifying all points on an equal-area grid in geocentric coordinates that lie within the geomagnetic polar caps (Figures 4a–b) or geocentric polar caps (Figures 4g–h). We then calculate χ at all of these points at

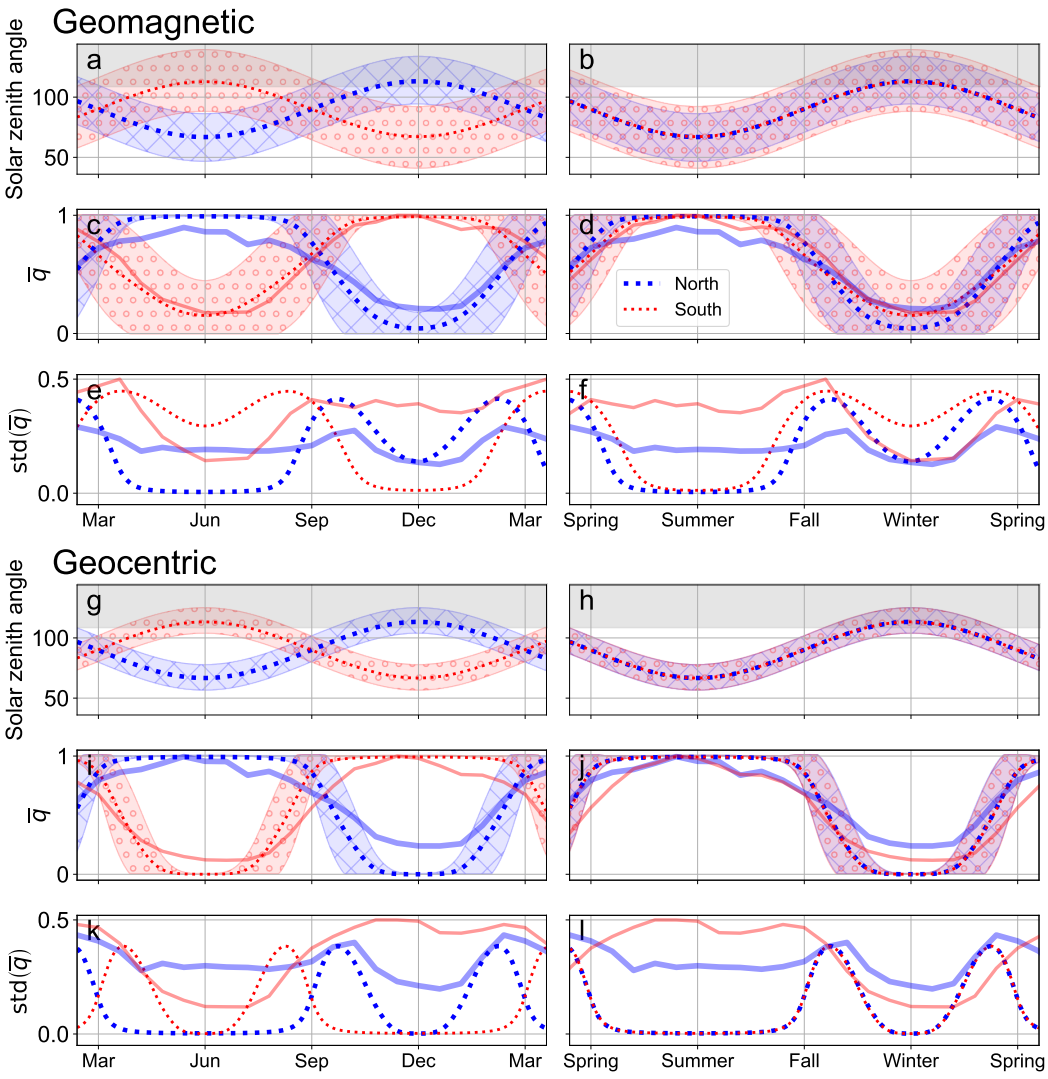

Figure 4. Daily average, minimum, and maximum of solar zenith angle χ (Figures 4a–b and g–h) and the plasma production model given by Equation (4) (Figures 4c–f and i–l) versus season parameter ϕ_s (season in the left panels and local season in the right panels; see section 3.1) in the Northern (blue) and Southern Hemisphere (red) geomagnetic polar caps (three upper rows, Figures 4a–f) and geocentric polar caps (three lower rows, Figures 4g–l). Tick marks in each panel precisely indicate the relevant equinox or solstice. The average (panels a–d and g–j) or standard deviation (panels e–f and k–l) of each quantity is indicated by a thick dotted line (NH) and thin dotted line (SH). The average plus or minus one standard deviation in panels a–d and g–j is indicated by cross and circle hatching for the Northern and Southern Hemisphere, respectively. The gray shading in the upper half of panels a–b and e–f indicates the range of χ values above the maximum solar zenith angle χ_m ($\chi_m \approx 108.6°$) at which the Sun is visible at 350-km altitude according to Equation (1). The solid blue (NH) and red (SH) lines in Figures 4c–f are median geomagnetic polar cap N_e^* (Figures 4c–d) and MAD(N_e^*) (Figures 4e–f), taken and scaled from Figures 2a–d. The corresponding lines in Figures 4i–l are median geocentric polar cap N_e^* (Figures 4i–j) and MAD(N_e^*) (Figures 4k–l).

30-minute intervals. We have calculated these ranges for each day during one year. Daily average χ values are indicated by thick dotted blue (NH) and thin dotted red (SH) lines, with daily minimum and maximum χ values indicated by the envelopes with cross (NH) and circle (SH) hatching.

These ranges indicate that in the geomagnetic polar caps, average χ values as a function of local season are very similar (Figure 4b). However, as expected, χ values within the SH geomagnetic polar cap span a larger range than χ values in the NH geomagnetic polar cap. On the other hand, and as expected, in the geocentric polar caps the ranges of χ values as a function of local season are essentially identical (Figure 4h).

To investigate the role of solar illumination in polar cap plasma production, we assume a simple model for polar cap plasma production of the form

$$\overline{P}\left(h,\chi\right)=\frac{P\left(h,\chi\right)}{I_{\infty}\eta\sigma^{a}}=\exp\left[-\tau\left(h,\chi\right)\right]n(h), \tag{2}$$

which depends on the altitude h and solar zenith angle χ. The production function $\overline{P}$ is the number of electron-ion pairs produced per unit volume per unit time $P\left(h,\chi\right)$, per photon flux at infinity I_{∞}, per probability of photon absorption η, per absorption cross section σ^{a}. The factors $\tau\left(h,\chi\right)$ and $n(h)\ =\ n_{0}e^{-(h-h_{0})/H_{n}}$ are respectively the optical depth and the exponential number density profile of a single-species neutral atmosphere in thermal and hydrostatic equilibrium, with neutral scale height H_{n}. The optical depth $\tau\left(h,\chi\right)=H_{n}n(h)\sigma^{a}\mathrm{Ch}\left(h,\chi\right)$, where (e.g., Chapman, 1931; Rees, 1989; Huestis, 2001)

$$\mathrm{Ch}\left(h,\chi\right)=\begin{cases}\mathrm{Ch}^{*}\left(h,\chi\right)\equiv\frac{1}{H_{n}}\int_{h}^{\infty}dh'\left\{\frac{\exp\left[-(h'-h)/H_{n}\right]}{\sqrt{1-\left(\frac{R+h}{R+h'}\right)^{2}\sin^{2}\chi}}\right\}; & \chi\leq\frac{\pi}{2}\\ 2\mathrm{Ch}^{*}\left(h\sin\left[\pi-\chi\right],\frac{\pi}{2}\right)-\mathrm{Ch}^{*}\left(h,\chi\right); & \frac{\pi}{2}<\chi<=\chi_{m}\\ \infty. & \chi>\chi_{m}\end{cases} \tag{3}$$

The function $\mathrm{Ch}\left(h,\chi\right)$ describes the attenuation of monochromatic radiation in a radial, single-species exponential atmosphere. More specifically $\mathrm{Ch}\left(h,\chi\right)$ is the unitless ratio of the actual column depth and the column depth for overhead Sun (i.e., $\chi=0$) at altitude h for a spherical Earth.

Figure 5 shows on logarithmic scales the optical depth τ (left panel), and the plasma production $\overline{P}$ in Equation (2) normalized by the plasma production at 235-km altitude and $\chi=0$, which is the altitude of maximum plasma production (right panel). For these

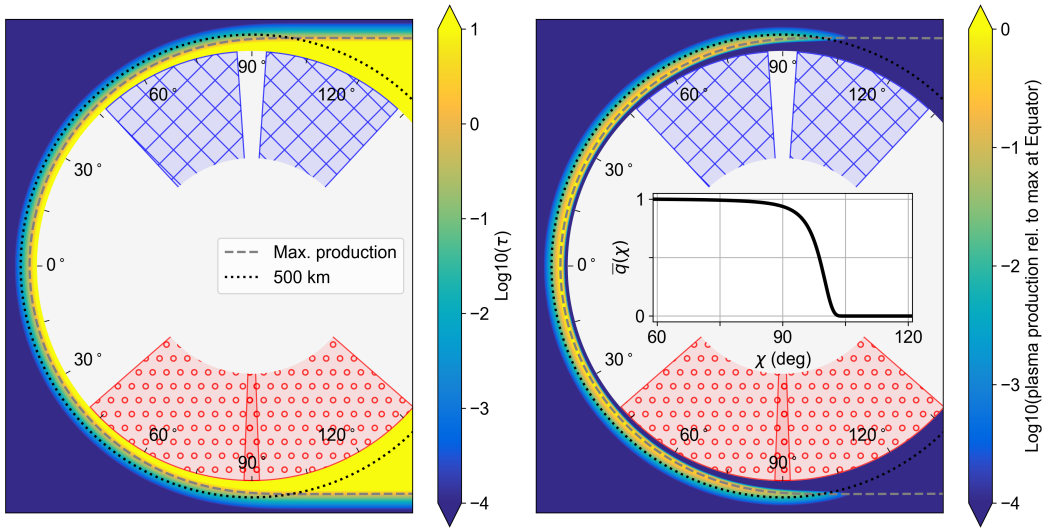

Figure 5. Optical depth $\tau\,(h,\chi) = H_n n(h)\sigma^a \mathrm{Ch}\,(h,\chi)$ (left panel), and the plasma production $\overline{P}$ in Equation (2) normalized by the plasma production at the altitude of maximum plasma production, 235 km, for $\chi = 0$ (right panel). For these plots we use $H_n = 50$ km, $n(h) = n_0 e^{-(h-h_0)/H_n}$ with $n_0 = 10^7$ cm^{-3} at a reference altitude $h_0 = 500$ km, and $\sigma^a = 1 \times 10^{-20}$ m^2. Both quantities are shown on logarithmic scales. In each panel the dashed gray line indicates the altitude of maximum plasma production, and the dotted black line indicates an altitude of 500 km. The hatched regions indicate the minimum and maximum solar zenith angles at June solstice and December solstice for the geomagnetic polar caps (see also Figure 4a). The normalized production function $\overline{q}\,(\chi)$ in Equation (4) is shown in the inset plot in the right panel.

calculations we use $H_n = 50$ km, and $\sigma^a = 1 \times 10^{-20}$ m^2. The value of H_n is chosen by assuming $H_n = \frac{kT_n}{m_n g}$, with T_n =950 K, m_n =16 amu, and g =9.8 m/s^2. We also assume $n_0 = 10^7$ cm^{-3} at a reference altitude $h_0 = 500$ km (e.g., Chapter 9 of Schunk & Nagy, 2009; Fennelly & Torr, 1992). At h_0 the optical depth is thus $\tau_0 = \tau(h_0, 0) = 5 \times 10^{-3}$. In each panel the altitude of maximum plasma production and an altitude of 500 km are indicated respectively by the dashed gray line and the dotted black line. The hatched regions indicate the minimum and maximum solar zenith angles at June solstice and December solstice for the geomagnetic polar caps from Figure 4a.

To examine the effects of seasonal variations in geomagnetic polar cap plasma production with the model given by Equation (2), we further define the normalized plasma production function at h_0

$$\bar{q}(\chi) \equiv \frac{\overline{P}(h_0, \chi)}{\overline{P}(h_0, 0)} = \exp\left[\tau_0 \left(1 - \mathrm{Ch}(h_0, \chi)\right)\right], \tag{4}$$

which is the number of electron-ion pairs produced per unit volume, normalized relative to the production function $\overline{P}(h_0, 0)$ for overhead Sun at reference altitude h_0. The function $\bar{q}(\chi)$ is similar in form to the non-normalized "Chapman production function" given by Equation 9.21 in Schunk and Nagy (2009), with the factor $\sec\chi$ in the exponent replaced by $\mathrm{Ch}(h_0, \chi)$. The normalized production function $\overline{q}(\chi)$ is shown in the inset plot in the right panel of Figure 5. Incidentally the "flat-Earth" plasma production model of ideal Chapman theory (e.g., Schunk & Nagy, 2009; Ieda et al., 2014), which predicts that the maximum plasma density is proportional to $\sqrt{\cos\chi}$, is obtained for $R \to \infty$ in Equations (1) and (3).

Swarm and CHAMP N_e^* measurements uniformly sample geocentric latitude, which implies that the number of N_e^* measurements per unit area increases with increasing geocentric latitude λ^{gc}. To approximately account for increasing sampling with increasing λ^{gc} in the plasma production model $\overline{q}(\chi)$ we weight each equal-area grid point by $\cos(\lambda^{\mathrm{gc}})$. This weighting produces small differences of no more than 0.07 and typically less than 0.03 in the average $\bar{q}$ value.

Figures 4c–d show the daily average $\bar{q}$ values for the geomagnetic polar caps, and Figures 4i–j show corresponding values for the geographic polar caps. The NH and SH averages are respectively indicated by the thick dotted blue line and thin dotted red line. The transparent envelopes with cross and circle hatching respectively indicate the average NH and SH $\bar{q}$ values plus or minus one standard deviation. The envelopes are nec-

essarily within the range $[0, 1]$. For reference, the thick blue and thin red lines in Figures 4c–d indicate median NH and SH geomagnetic polar cap N_e^*, respectively, taken and scaled from Figures 2a and c. These lines are scaled such that $\bar{q} = 0$ corresponds to median $N_e^* = 0$, and $\bar{q} = 1$ corresponds to the maximum value of median SH $N_e^*(\approx 8 \times 10^4 \mathrm{cm}^{-3})$. From these figures it is apparent that seasonal variations in median N_e^* very roughly follow the seasonal variations of the production function $\bar{q}$, with the lowest median N_e^* values occurring within the portions of the year during which average $\bar{q}$ values are lowest and vice versa.

A more detailed comparison of average $\bar{q}$ values in Figure 4c at March equinox reveals that the average $\bar{q}$ is greater in the NH than in the SH. In contrast, the median N_e^* at March equinox is less in the NH than in the SH. At September equinox the average $\bar{q}$ is greater in the NH than in the SH; median N_e^* values at September equinox, however, do not indicate evidence of a hemispheric asymmetry.

In summary, the illumination model predicts plasma densities that are greater in the NH geomagnetic polar cap than in the SH geomagnetic polar cap during both March and September equinox. Median N_e^* values at each equinox do not support this model prediction.

Figure 4d, which shows $\bar{q}$ statistics and median N_e^* as a function of local season, reveals that $\bar{q}$ is overall higher in the NH geomagnetic polar cap than in the SH geomagnetic polar cap around both local spring equinox and local fall equinox. Median N_e^* values are likewise higher in the NH geomagnetic polar cap around local spring equinox, which is consistent with the model prediction. Around local fall equinox, however, median N_e^* values are higher in the SH geomagnetic polar cap, which is inconsistent with the model prediction. Figure 2c indicates that the larger NH spring and SH fall densities are apparently a consequence of the lag in SH geomagnetic polar cap median N_e^* at local spring and fall equinox.

To assess whether the differences identified above between $\bar{q}$ statistics and median N_e^* are related to a choice of coordinate system Figures 4i and 4j show $\bar{q}$ statistics and median N_e^* for the geocentric polar caps. These lines are obtained by performing the scaled season parameter analysis of section 3.1 using Swarm and CHAMP N_e^* measurements made within the geocentric polar caps (see Table 2) instead of the geomagnetic polar caps.

Figure 4i shows that the illumination model predicts equal production of plasma (assuming identical neutral atmospheres) in each geocentric polar cap at March and September equinox. In contrast, the median N_e^* at both equinoxes is higher in the NH geocentric polar cap than in the SH geocentric polar cap. Thus the illumination model is inadequate to describe the observed asymmetric median N_e^* values around March and September equinoxes.

As expected from Figure 4i, Figure 4j shows that the illumination model predicts equal production of plasma (assuming identical neutral atmospheres) in each geocentric polar cap at each local equinox. The median N_e^* at local spring equinox in Figure 4j is, in contrast, significantly higher in the NH geocentric polar cap than in the SH geocentric polar cap, but approximately equal in each polar cap around local fall equinox. The illumination model is thus inadequate to describe the observed asymmetries in the median N_e^* around local spring equinox also if we consider the geocentric polar caps.

Finally, Figure 4e compares the standard deviation of $\bar{q}$ values (dotted lines), denoted std($\bar{q}$), with MAD(N_e^*) values (solid transparent lines) taken from Figure 2b. The two peaks in NH MAD(N_e^*) that occur before and after December solstice are near the two peaks in std($\bar{q}$). Similarly, the peak and plateau in SH MAD(N_e^*) that occur before and after June solstice, respectively, appear to correspond to the two peaks in SH std($\bar{q}$).

Figure 4f compares the same quantities as a function of local season. In this figure it is clear that the minimum std($\bar{q}$) and the minimum MAD(N_e^*) in each hemisphere both occur near local winter, and both quantities evince peaks near local spring and fall equinoxes. However, from local spring equinox to local fall equinox the values of MAD(N_e^*) are nonzero, whereas the plasma production model predicts std($\bar{q}$) ≈ 0 around local summer solstice.

Figures 4k–l show std($\bar{q}$) and MAD(N_e^*) for the geocentric polar caps. Similar to the NH geomagnetic polar cap, the two peaks in MAD(N_e^*) for the NH geocentric polar cap occur near the peaks in std($\bar{q}$). In contrast, in the SH geocentric polar cap the primary commonality between MAD(N_e^*) and std($\bar{q}$) is that both quantities are larger during December solstice (local summer) than during June solstice (local winter). There are otherwise no obvious similarities between MAD(N_e^*) and std($\bar{q}$) in the SH geocentric polar cap.

Table 2. Equinoctial asymmetries in median adjusted geomagnetic polar cap plasma density N_e^* identified in this study.

Asymmetry	(Fig)	Δt (all sat.) days	Δt (individ. sat.)[a] days
NH/SH Mar crossover delay	(1a)	4.0	[2.3, 0.4, 10.0, 6.0]
NH/SH Sep crossover[b]	(1a)	0.4	[1.0, −0.4, 0.4, −2.3]
NH spring/fall crossing	(3a)	−7.2	[−9.7, −7.6, −6.0, −7.3]
SH spring/fall crossing	(3b)	9.1	[8.3, 6.5, 14.2, 8.4]
NH/SH spring crossing	(3c)	18.0	[19.1, 16.7, 19.3, 17.4]
NH/SH fall crossing	(3d)	57.8[c]	[26.2, 57.8, 60.0, 58.7]

[a] [CHAMP, Swarm A, Swarm B, Swarm C].

[b] Evidence for this asymmetry is weak, as Δt is small and exhibits spread around zero.

[c] As indicated in section 3.2, median N_e^* in the NH and SH are within a few percent of each other over days 30 to 60 after equinox.

Whereas the solar EUV flux does not (or seldom) vary from day to day, aside from during solar flares and modulation related to solar rotation, electron impact ionization in the auroral and polar cap ionosphere does. Therefore from local fall to local spring, when solar EUV flux contributes less to plasma production (and at local winter solstice contributes almost nothing), the overall variation in plasma production relative to the mean magnitude of the production is therefore larger. It is therefore interesting to examine the "relative plasma density variation" [MAD(N_e^*)/median(N_e^*)] (Figure S2 in Supporting Information). This quantity reaches a maximum around local winter and a minimum around local summer in both the NH and SH geomagnetic polar caps. The relative plasma density variation shows the same behavior when calculated using the geocentric polar cap. Likewise the quantity std($\bar{q}$)/$\bar{q}$ (Figures S2e–f and Figures S2k–l) reaches a maximum at local winter solstice and a minimum at local summer solstice in the NH and SH polar caps, for both geomagnetic and geocentric polar caps.

5 Discussion

Results in the preceding sections indicate the existence of several seasonal and hemispheric asymmetries in the plasma density of the geomagnetic polar caps. Table 2 summarizes the equinoctial asymmetries identified from Figures 1–3 on the basis of the combined database of Swarm and CHAMP measurements.

The most significant results of analysis in section 3 are displayed in Figure 3. In Figure 3a the crossover point of the two Northern Hemisphere (solid blue) lines occurs approximately 7 days before equinox, whereas in Figure 3b the crossover point of the two Southern Hemisphere (dotted red) lines occurs approximately 9.1 days after equinox. Thus the days on which the local hemisphere geomagnetic polar cap density N_e^* crossover near local equinox occurs are hemispherically asymmetric. This asymmetry is also present when the polar caps are defined in geocentric coordinates (not shown), and so is not the result of a particular choice of coordinate system.

Comparison of median N_e^* curves from each geomagnetic polar cap around local spring (Figure 3c) and around local fall (Figure 3d) shows that the crossover points in both hemispheres occur more than two weeks after equinox. This suggests the existence of a seasonal "phase offset" between the two hemispheres in median N_e^* around local spring and fall equinoxes, whereby N_e^* in the SH geomagnetic polar cap lags N_e^* in the NH geomagnetic polar cap by at least two weeks. Median N_e^* curves from each geocentric polar cap around local spring equinox (Figure 4j) exhibit a similar, even more pronounced lag, whereby N_e^* in the SH geocentric polar cap lags N_e^* in the NH geocentric polar cap by six weeks or more.

Thus the relative lag between SH and NH polar cap N_e^* around local spring equinox is not the result of choosing a particular definition of the polar caps (i.e., geomagnetic or geocentric polar caps; see Table 2). On the other hand there is apparently no lag between SH and NH geocentric polar cap N_e^* around local fall equinox, which suggests that the relative lag exhibited by N_e^* in the geomagnetic polar caps is related to the choice of coordinate system (i.e., geomagnetic instead of geocentric polar caps). The different lags imply that there are at least two contributing factors to the delay, which likely operate somewhat differently in the two sets of polar caps during local spring and local fall. Here it is worth noting that the existence of a relative lag in geomagnetic polar cap N_e^* around local fall equinox may be related to reported hemispheric asymmetry in ion out-

flow processes and ionosphere-magnetosphere coupling that is organized by the geomagnetic field (Haaland et al., 2012; André et al., 2015; Haaland et al., 2017).

To test the robustness of the asymmetries identified in Figures 1–3 and Table 1, we have also performed the analysis separately for each of the four satellites used in this study (not shown). The values obtained from each of these separate analyses are shown in the rightmost column of Table 2. All of the asymmetries we have just discussed also appear in the analyses based on measurements from individual satellites. More specifically with the exception of the weak evidence for a NH/SH crossover delay at September equinox, the other delays are consistent between all four spacecraft albeit with slight differences in the estimated Δt values.

We believe these separate analyses are important indicators of the robustness of each asymmetry, since the Swarm and CHAMP satellites monitor polar cap plasma density at effectively three different altitude ranges over two different portions of a solar cycle, with two different and independent types of Langmuir probe instruments and three different orbits.

To understand whether these observed asymmetries can be explained solely on the basis of differences in solar illumination, in section 4 we have used an illumination-dependent plasma production model with representative values of parameters such as neutral temperature and absorption cross section. More significant than any of the chosen values of these neutral atmosphere parameters, however, is our much more basic (and unrealistic) assumption of a neutral atmosphere that consists of a single species, a single wavelength-independent absorption cross section, and a constant temperature profile that does not vary with season.

One purpose of this study is to determine whether the hemispheric asymmetry in magnetospheric lobe cold plasma density reported by Haaland et al. (2017) could be explained on the basis of plasma densities in the ionospheric polar caps. In specific, they found that the distribution of densities in the NH lobe were overall greater than the distribution of densities in the SH lobe around September equinox, and speculated whether this asymmetry was due to differences in outflow and plasma densities between NH and SH. No such corresponding asymmetry in median geomagnetic polar cap N_e^* at September equinox is apparent in Figures 1a and 2a. There is, however, evidence of a corresponding asymmetry in the median geographic polar cap N_e^* (Figure 4i).

Other possible causes of the asymmetry in cold plasma density could therefore be hemispherically asymmetric vertical transport, flux tube volume, or conductivities in the geomagnetic polar caps. Li et al. (2020) have shown, for instance, that the strength of the Earth's magnetic field is anti-correlated with ionospheric outflow. The cause of this apparent discrepancy between Swarm, CHAMP, and Cluster observations will be the subject of future work.

6 Summary

Using 15 years of plasma density measurements made by the original three Swarm satellites and the CHAMP satellite, we have identified equinoctial asymmetries in F-region ionosphere plasma density in the geomagnetic polar caps. In particular we present evidence that SH polar cap plasma density lags behind NH polar cap plasma density by at least two weeks. We have used a simplistic plasma production model based on solar illumination to show that the observed asymmetries are likely not the result of differences in solar illumination between the two polar caps.

Appendix A Correction and Adjustment of N_e

As mentioned in section 2, we apply the Lomidze et al. (2018) calibrations

$$N_e = \nu_\alpha^2 \, N_{e,\alpha}. \tag{A1}$$

to Swarm plasma density measurements. Here N_e is the flight-calibrated plasma density measurement, α indexes the three Swarm satellites, $N_{e,\alpha}$ is the plasma density measured by the LP instrument, and ν_α is one of the three satellite-dependent correction factors

$$\nu_A = 1.1067;$$

$$\nu_B = 1.0882;$$

$$\nu_C = 1.1157.$$

We additionally account for differences in altitude and solar activity via (i) application of an empirically derived scale height to N_e measurements that "maps" N_e to a common geodetic altitude of 500 km, and (ii) application of an empirically derived correction factor that accounts for the variation of N_e measurements with 10.7-cm solar radio flux (otherwise known as the $F10.7$ index).

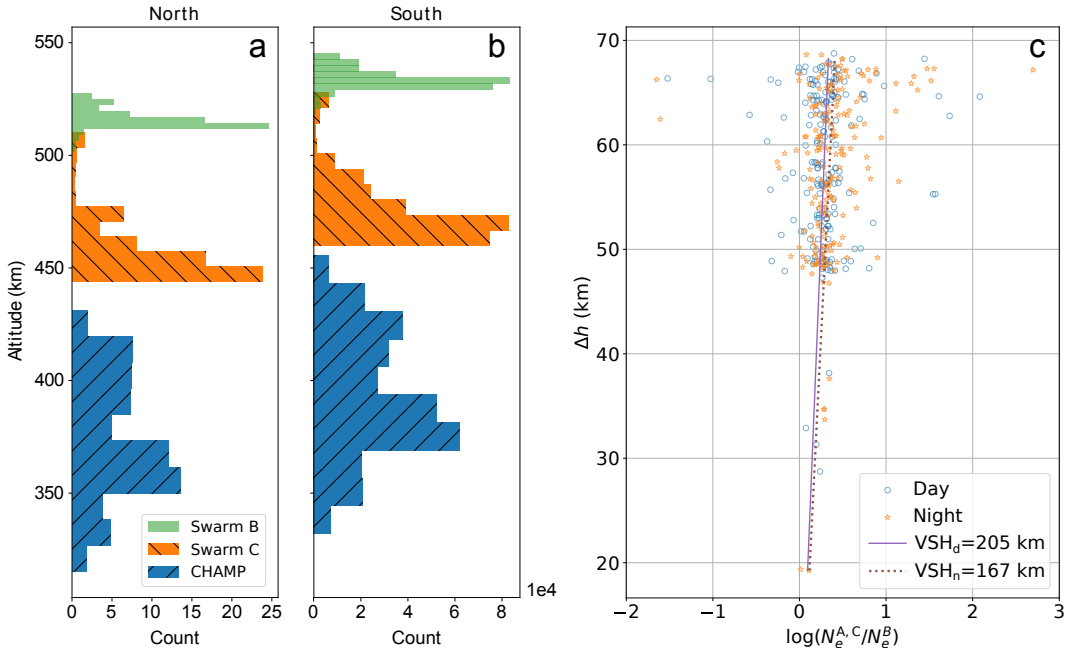

Figure A1. Panels a and b show geodetic altitude distributions of Swarm B (green), Swarm C (orange), and CHAMP (blue) satellites in the NH and SH geomagnetic polar caps above 80° MLat, respectively. (The altitude distribution of Swarm A is essentially identical to Swarm C and is not shown.) Panel c shows empirical Vertical Scale Height (VSH) estimates based on 380 conjunctions (see text for definition) between Swarm B and one of the two satellites at lower altitudes (either Swarm A or Swarm C) in the period from 10 Dec 2013 and 6 Feb 2020 for which Swarm LP measurements are available. The x axis indicates the logarithm of the ratio of Lomidze et al. (2018)-corrected plasma density measurements, and the y axis indicates the spacecraft altitude separation. The circle and star markers respectively denote dayside (6–18 MLT) and nightside (18–6 MLT) conjunctions.

A1 Adjustment of N_e for Altitude Variations

As pointed out in section 2 the CHAMP satellite and the three Swarm satellites cover different altitude ranges, and thus different portions of the F region. Figures A1a–b display the geodetic altitude coverage of each satellite in the NH and SH geomagnetic polar cap. The altitude range covered by the CHAMP satellite (315–455 km) is the lowest of all four satellites, while the altitude range covered by Swarm B (500–545 km) is mostly above those of the other satellites. The narrow range of geodetic altitudes 501–510 km in the NH geomagnetic polar cap (518–527 km in the SH geomagnetic polar cap) where Swarm B and Swarm C overlap represents the initial Swarm flight configuration

when all three satellites flew at approximately 500-km geodetic altitude in the NH (520-km geodetic altitude in the SH). The orbit of Swarm B was later boosted to higher altitudes, while the orbits of Swarm A and Swarm C were lowered. (The altitude distribution covered by Swarm A is not shown since it and Swarm C have followed very similar orbital trajectories since launch.)

Comparison of the geodetic altitude distributions in each hemisphere indicates a systematic difference in each satellite's range of altitudes: in each case the NH geomagnetic polar cap distribution of altitudes is systematically offset by approximately 20 km relative to the SH geomagnetic polar cap distribution. This is due to the combined effects of the Earth's oblateness and the slightly elliptical orbit of each satellite.

From 380 conjunctions between Swarm B and either Swarm A or Swarm C for which Swarm LP data is currently available (Dec 2013 through Feb 2020) we derive an empirical scale height. These conjunctions were identified via the Query tool (`https://sscweb.gsfc.nasa.gov/cgi-bin/Query.cgi`) at NASA's Satellite Situation Center Web (`https://sscweb.gsfc.nasa.gov/`) by requiring a horizontal separation of less than 100 km after radially tracing the footpoint of each satellite to a common altitude.

For each conjunction identified by the Query tool, we use a 10-minute window to calculate the time at which the angular separation

$$\Delta\zeta = \arccos\left[\sin\lambda_1^m \sin\lambda_2^m + \cos\lambda_1^m \cos\lambda_2^m \cos\left(\mid \theta_1 - \theta_2 \mid\right)\right], \tag{A2}$$

between the two satellites is a minimum. Here λ^m and θ respectively denote MLat and geomagnetic longitude in MA_{110} coordinates. We then use this more precise list of conjunction times to calculate the Vertical Scale Height VSH $\equiv dh/(d\ln N_e)$ (e.g., Hu et al., 2019).

Each conjunction corresponds to a single point in Figure A1c, which shows the logarithm of the ratio of N_e measurements made by Swarm B and either Swarm A or Swarm C on the x axis, and the altitude separation Δh in kilometers between the satellite pair on the y axis. The circle and star markers respectively denote dayside (6–18 MLT) and nightside (18–6 MLT) conjunctions. The spread in the logarithm of density ratios on the x axis indicate overall significant variability in the plasma density at each altitude. This spread is not surprising given the various contributions to density made by, for example, plasma convection, polar cap patches, and auroral precipitation. On the other hand,

individual points in Figure A1c also indicate the existence of a particular scale height, or an approximately linear relationship between altitude difference and the logarithm of the ratio of plasma density at each altitude.

We use so-called "robust regression" to estimate the VSH from measurements in Figure A1c. In specific we perform an iterative Huber-weighted least-squares linear regression (e.g., Huber (1973); Holland and Welsch (1977)) to data in Figure A1c with the function

$$\log\left(N_e^{\mathrm{A,C}}/N_e^{\mathrm{B}}\right) = \beta\Delta h, \tag{A3}$$

where $\beta \equiv 1/\mathrm{VSH}$. We use the `HuberRegressor` module of the `Scikit-learn` Python package (Pedregosa et al., 2011) with $\epsilon = 1.5$. The ϵ parameter in Huber-weighted iterative regression controls the degree to which the regression is sensitive to outlier points.

From this regression we obtain the purple and brown lines, which respectively correspond to VSH= 205 km on the "dayside" and VSH= 167 km on the "nightside." We use magnetic local time (MLT) in MA_{110} coordinates to define "dayside" as $6 \leq \mathrm{MLT} < 18$, and "nightside" as $\mathrm{MLT} < 6$ and $\mathrm{MLT} \geq 18$. These VSH values are within the range of typical estimates at geodetic altitudes of 350–500 km (see, e.g., Figure 2 in Hu et al. (2019) and Figure 1B in Stankov and Jakowski (2006)). To each N_e measurement we then apply a scaling factor

$$N_{e,h_0} = N_e \exp\left[(h - h_0)/\mathrm{VSH}\right], \tag{A4}$$

where h is the altitude at which the measurement is made and VSH is the empirical scale height. We arbitrarily select a reference geodetic altitude $h_0 = 500$ km. This scaling decreases the value of N_e for measurements made below h_0 and increases the value of N_e for measurements made above h_0.

A2 Adjustment of N_e for $F10.7$ Variations

In addition to variation with altitude, polar cap N_e also varies with the intensity of sunlight. We use an average of the $F10.7$ index during the preceding 27 days, denoted by $\langle F10.7\rangle_{27}$, as a proxy for solar EUV intensity. (The $F10.7$ index is publically available via the NASA OMNI database at `https://omniweb.gsfc.nasa.gov/form/dx1.html`.) Another common choice for averaging the $F10.7$ index is a centered 81-day window (e.g., L. Liu & Chen, 2009; Schunk & Nagy, 2009). We have elected to use $\langle F10.7\rangle_{27}$ instead,

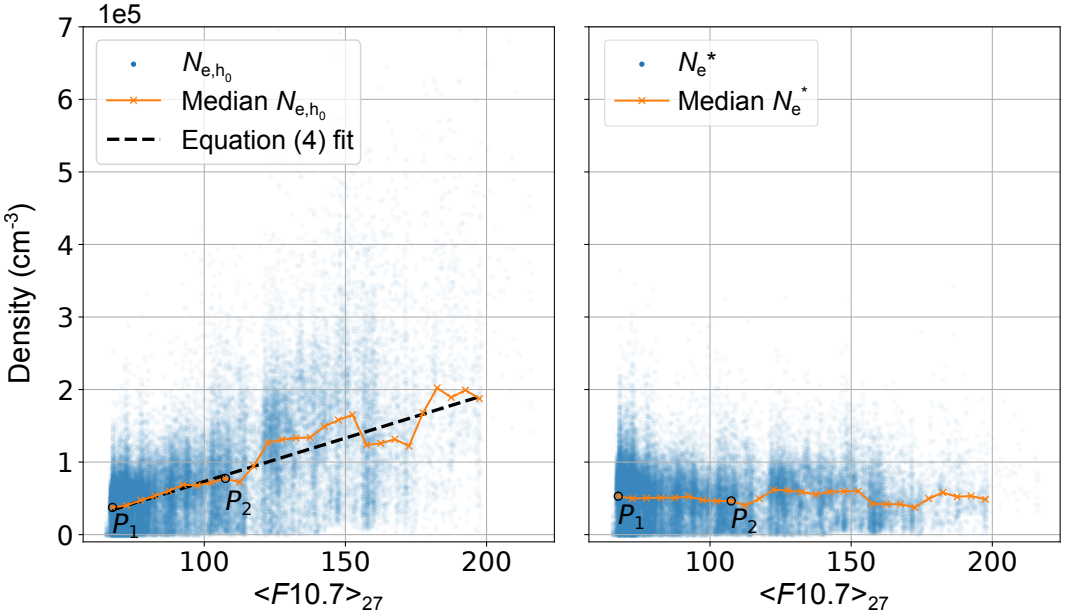

Figure A2. Height-scaled plasma densities before (left) and after (right) adjusting for variation in $\langle F10.7\rangle_{27}$ using Equation (A6). In the left panel the black dashed line indicates the model given by Equation (A5) with best-fit parameters $a = 0.02564$ and $N = 46{,}780$ obtained by performing the iterative Huber-weighted least-squares nonlinear regression described in the text. The two points P_1 and P_2 indicate the two points used to obtain initial estimates for model parameters a and N, and are shown in the right panel to indicate the effect of applying Equation (A6) to N_{e,h_0} values. In both panels the orange line indicates the median value, N_{e,h_0} in the left panel and N_e^{adj} in the right panel, within $\langle F10.7\rangle_{27}$ bins of 5.

since we find that the RMS error between $\langle F10.7\rangle_{27}$ and N_{e,h_0} is slightly ($\sim$5%) lower than the RMS error between an 81-day centered average of the $F10.7$ index and N_{e,h_0}.

Figure A2a shows height-scaled polar cap N_{e,h_0} plotted versus $\langle F10.7\rangle_{27}$. The orange line indicates median N_{e,h_0} values within bins of 5 for $\langle F10.7\rangle_{27}$ between 65 and 200. The variation of median N_{e,h_0} with $\langle F10.7\rangle_{27}$ is approximately linear.

To scale N_{e,h_0} measurements for variation with $F10.7$, we perform an iterative Huber-weighted least-squares linear regression to all 3,456,077 N_{e,h_0} values with a model of the form

$$N_{e,h_0} = A\langle F10.7\rangle_{27} - B = N\left(a\langle F10.7\rangle_{27} - 1\right). \tag{A5}$$

In practice the actual best-fit parameters are not sensitive to our choice of initial parameter estimates, but for illustrative purposes we use the two points indicated in Figure A2a, $P_1 = (F_1, N_1) = (67.5, 37516)$ and $P_2 = (F_2, N_2) = (107.5, 77460)$ together with the model in Equation (A5) to obtain the initial model estimates $\hat{A} = (N_2 - N_1)/(F_2 - F_1) = 999$ and $\hat{B} = \hat{N} = \hat{A}F_1 - N_1 = 29890$, such that $\hat{a} = \hat{A}/\hat{B} = 0.033$.

The resulting best-fit model parameters with weighting parameter $\epsilon = 1.5$ are $a = 0.02564$ and $N = 46,780$; the resulting model of the form given by Equation (A5) is indicated by the black dashed line in Figure A2a. These fit parameters are obtained by requiring that the relative change in each model parameter be less than 10^{-8} after each iteration, which is generally acheived after 35–60 iterations. We apply the portion of the model in Equation (A5) that is dependent on $\langle F10.7\rangle_{27}$, namely the parameter a, to each N_{e,h_0} value to finally obtain the height- and solar flux-adjusted density

$$N_e^* = N_{e,h_0}\frac{80a - 1}{a\langle F10.7\rangle_{27} - 1}. \tag{A6}$$

The numerator in Equation (A6) scales the final adjusted density N_e to a nominal solar flux level of $\langle F10.7\rangle_{27} = 80$. These final adjusted densities are shown in Figure A2b.

Appendix B 95% Confidence Interval of the Median

The 95% confidence interval of each median displayed in Figure 1a is calculated in each DOY bin by first sorting the N_e^* values in that DOY bin, and then identifying the value of N_e^* corresponding to the Lth and Uth sorted sample in that DOY bin. These

sorted sample numbers are given by (Conover, 1999)

$$L = \lfloor Q_b(0.025, N, 0.5) \rfloor; \qquad U = \lceil Q_b(0.975, N, 0.5) \rceil; \tag{B1}$$

where $\lfloor\rfloor$ and $\lceil\rceil$ are respectively floor and ceiling functions and $Q_b(p, N, q)$ is the quantile function, otherwise known as the "inverse cumulative distribution" or "percent-point function," of the binomial distribution. The parameters of this quantile function are the probability p, the number of observations N, and the quantile of interest q. We use $p = 0.025, 0.975$ corresponding to the 95% confidence interval, and $q = 0.5$ corresponding to the 50% quantile or median. We calculate $Q_b(p, N, q)$ via the `stats.binom.ppf` method of the `scipy` Python package (Virtanen et al., 2020).

Acknowledgments

Work at the Birkeland Center for Space Science and the University of Bergen was funded by the Research Council of Norway/CoE under contract 223252/F50 and by ESA contract 4000126731 in the framework of EO Science for Society.

The Level 2 CHAMP PLP dataset and Level 1B Swarm LP dataset are publically accessible via `ftp://isdcftp.gfz-potsdam.de` and `https://swarm-diss.eo.esa.int/`, respectively. The $F10.7$ index is available via the NASA OMNI database (`https://omniweb.gsfc.nasa.gov/form/dx1.html`)

References

Adams, G. W., & Masley, A. J. (1965, Mar). Production rates and electron densities in the lower ionosphere due to solar cosmic rays. *Journal of Atmospheric and Terrestrial Physics*, *27*(3), 289-298. doi: 10.1016/0021-9169(65)90029-2

André, M. (2015, Dec). Previously hidden low-energy ions: a better map of near-Earth space and the terrestrial mass balance. *Physica Scripta*, *90*(12), 128005. doi: 10.1088/0031-8949/90/12/128005

André, M., Li, K., & Eriksson, A. I. (2015, Feb). Outflow of low-energy ions and the solar cycle. *Journal of Geophysical Research (Space Physics)*, *120*(2), 1072-1085. doi: 10.1002/2014JA020714

Appleton, E. V. (1939, July). Characteristic variation of region f_2 ionization throughout the year. *Nature*, *144*(3638), 151-152. doi: 10.1038/144151a0

672 Appleton, S. E. (1956, Jan). Regularities and irregularities in the ionosphere. *Vistas*
673 *in Astronomy*, *2*(1), 779-790. doi: 10.1016/0083-6656(56)90001-0
674 Aruliah, A. L., Farmer, A. D., Fuller-Rowell, T. J., Wild, M. N., Hapgood, M., &
675 Rees, D. (1996, July). An equinoctial asymmetry in the high-latitude thermo-
676 sphere and ionosphere. *jgr*, *101*, 15713-15722. doi: 10.1029/95JA01102
677 Aruliah, A. L., Farmer, A. D., Rees, D., & Brändström, U. (1996, July). The sea-
678 sonal behavior of high-latitude thermospheric winds and ion velocities observed
679 over one solar cycle. *Journal of Geophysical Research: Space Physics*, *101*,
680 15701-15712. doi: 10.1029/96JA00360
681 Axford, W. I. (1968, November). The polar wind and the terrestrial helium budget.
682 *J. Geophys. Res.*, *73*, 6855-6859. doi: 10.1029/JA073i021p06855
683 Banks, P. M., & Holzer, T. E. (1968). The polar wind. *Journal of Geophysical Re-*
684 *search*, *73*(21), 6846–6854. doi: 10.1029/JA073i021p06846
685 Bjoland, L. M., Belyey, V., Løvhaug, U. P., & La Hoz, C. (2016, sep). An evalu-
686 ation of International Reference Ionosphere electron density in the polar cap
687 and cusp using EISCAT Svalbard radar measurements. *Ann. Geophys.*, *34*(9),
688 751–758. doi: 10.5194/angeo-34-751-2016
689 Brekke, A. (1997). *Physics of the polar upper atmosphere*. Springer Nature.
690 Burns, A. G., Solomon, S. C., Wang, W., Qian, L., Zhang, Y., & Paxton, L. J.
691 (2012, sep). Daytime climatology of ionospheric N m F 2 and h m F 2 from
692 COSMIC data. *Journal of Geophysical Research: Space Physics*, *117*(A9). doi:
693 10.1029/2012JA017529
694 Chapman, S. (1931, jan). The absorption and dissociative or ionizing effect of
695 monochromatic radiation in an atmosphere on a rotating earth. *Proceedings of*
696 *the Physical Society*, *43*(1), 26–45. doi: 10.1088/0959-5309/43/1/305
697 Chappell, C. R., Giles, B. L., Moore, T. E., Delcourt, D. C., Craven, P. D., & Chan-
698 dler, M. O. (2000, April). The adequacy of the ionospheric source in supplying
699 magnetospheric plasma. *Journal of Atmospheric and Solar-Terrestrial Physics*,
700 *62*, 421-436. doi: 10.1016/S1364-6826(00)00021-3
701 Chappell, C. R., Moore, T. E., & Waite, J. H., Jr. (1987, June). The ionosphere as
702 a fully adequate source of plasma for the earth's magnetosphere. *J. Geophys.*
703 *Res.*, *92*, 5896-5910. doi: 10.1029/JA092iA06p05896
704 Chartier, A. T., Huba, J. D., & Mitchell, C. N. (2019, nov). On the Annual Asym-

metry of High-Latitude Sporadic F. *Space Weather*, *17*(11), 1618–1626. doi: 10.1029/2019SW002305

Cladis, J. B. (1986, September). Parallel acceleration and transport of ions from polar ionosphere to plasma sheet. *Geophys. Res. Letters*, *13*, 893-896. doi: 10.1029/GL013i009p00893

Cnossen, I., & Förster, M. (2016, January). North-south asymmetries in the polar thermosphere-ionosphere system: Solar cycle and seasonal influences. *Journal of Geophysical Research (Space Physics)*, *121*, 612-627. doi: 10.1002/2015JA021750

Conover, W. J. (1999). *Practical Nonparametric Statistics* (3rd ed.). John Wiley & Sons.

Dang, T., Wang, W., Burns, A., Dou, X., Wan, W., & Lei, J. (2017, jun). Simulations of the ionospheric annual asymmetry: Sun-Earth distance effect. *Journal of Geophysical Research: Space Physics*, *122*(6), 6727–6736. doi: 10.1002/2017JA024188

Dessler, A. J., & Michel, F. C. (1966, Mar). Plasma in the geomagnetic tail. *Journal of Geophysical Research: Space Physics*, *71*(5), 1421-1426. doi: 10.1029/JZ071i005p01421

Dungey, J. W. (1963, Jan). Interactions of solar plasma with the geomagnetic field. *Planetary and Space Science*, *10*, 233-237. doi: 10.1016/0032-0633(63)90020-5

Emmert, J. T., Richmond, A. D., & Drob, D. P. (2010, aug). A computationally compact representation of Magnetic-Apex and Quasi-Dipole coordinates with smooth base vectors. *Journal of Geophysical Research: Space Physics*, *115*(A8). doi: 10.1029/2010JA015326

Feldstein, I. I., Lyatskaya, A. M., Sumaruk, P. V., & Shevnina, N. F. (1975, Dec). Ionization of the F-layer of the ionosphere and variations of the magnetic field in the near-polar region. *Geomagnetism and Aeronomy*, *15*, 1021-1027.

Fennelly, J., & Torr, D. (1992, jul). Photoionization and photoabsorption cross sections of O, N2, O2, and N for aeronomic calculations. *Atomic Data and Nuclear Data Tables*, *51*(2), 321–363. doi: 10.1016/0092-640X(92)90004-2

Förster, M., Rentz, S., Köhler, W., Liu, H., & Haaland, S. E. (2008). IMF dependence of high-latitude thermospheric wind pattern derived from CHAMP

738 cross-track measurements. *Annales Geophysicae*, *26*(6), 1581–1595. doi:
739 10.5194/angeo-26-1581-2008

740 Friis-Christensen, E., Lühr, H., Knudsen, D., & Haagmans, R. (2008, jan). Swarm –
741 An Earth Observation Mission investigating Geospace. *Advances in Space Re-*
742 *search*, *41*(1), 210–216. doi: 10.1016/j.asr.2006.10.008

743 Haaland, S., Lybekk, B., Maes, L., Laundal, K., Pedersen, A., Tenfjord, P., ...
744 Snekvik, K. (2017, January). North-south asymmetries in cold plasma den-
745 sity in the magnetotail lobes: Cluster observations. *Journal of Geophysical*
746 *Research: Space Physics*, *122*, 136-149. doi: 10.1002/2016JA023404

747 Haaland, S., Svenes, K., Lybekk, B., & Pedersen, A. (2012, Jan). A survey of the
748 polar cap density based on Cluster EFW probe measurements: Solar wind and
749 solar irradiation dependence. *Journal of Geophysical Research (Space Physics)*,
750 *117*(A1), A01216. doi: 10.1029/2011JA017250

751 Holland, P. W., & Welsch, R. E. (1977, jan). Robust regression using iteratively
752 reweighted least-squares. *Communications in Statistics - Theory and Methods*,
753 *6*(9), 813–827. doi: 10.1080/03610927708827533

754 Horwitz, J. L., Ho, C. W., Scarbro, H. D., Wilson, G. R., & Moore, T. E. (1994).
755 Centrifugal acceleration of the polar wind. *Journal of Geophysical Research*,
756 *99*(A8), 15051. doi: 10.1029/94JA00924

757 Hu, A., Carter, B., Currie, J., Norman, R., Wu, S., Wang, X., & Zhang, K. (2019,
758 jun). Modeling of Topside Ionospheric Vertical Scale Height Based on Iono-
759 spheric Radio Occultation Measurements. *Journal of Geophysical Research:*
760 *Space Physics*, *124*(6), 4926–4942. doi: 10.1029/2018JA026280

761 Huber, P. J. (1973, sep). Robust Regression: Asymptotics, Conjectures and Monte
762 Carlo. *The Annals of Statistics*, *1*(5), 799–821. doi: 10.1214/aos/1176342503

763 Huestis, D. L. (2001). Accurate evaluation of the Chapman function for atmo-
764 spheric attenuation. *Journal of Quantitative Spectroscopy and Radiative Trans-*
765 *fer*, *69*(6), 709–721. doi: 10.1016/S0022-4073(00)00107-2

766 Ieda, A., Oyama, S., Vanhamäki, H., Fujii, R., Nakamizo, A., Amm, O., ... Nishi-
767 tani, N. (2014, dec). Approximate forms of daytime ionospheric conductance.
768 *Journal of Geophysical Research: Space Physics*, *119*(12), 10,310–397,415. doi:
769 10.1002/2014JA020665

770 Ivanov-Kholodnyy, G. S. (1962, Jan). Ionization of the Upper Atmosphere by Solar

771 Short-Wave Radiation. *Geomagnetism and Aeronomy*, *2*, 561.

772 Khocholava, G. M. (1977, Mar). On diffusion-recombination parameters in the F-
773 region of the ionosphere. *Journal of Atmospheric and Terrestrial Physics*, *39*,
774 389-391. doi: 10.1016/S0021-9169(77)90154-4

775 Klumpar, D. M. (1979, Aug). Transversely accelerated ions: An ionospheric source
776 of hot magnetospheric ions. *Journal of Geophysical Research: Space Physics*,
777 *84*(A8), 4229-4237. doi: 10.1029/JA084iA08p04229

778 Knudsen, D. J., Burchill, J. K., Buchert, S. C., Eriksson, A. I., Gill, R., Wahlund,
779 J., ... Moffat, B. (2017, feb). Thermal ion imagers and Langmuir probes in
780 the Swarm electric field instruments. *Journal of Geophysical Research: Space*
781 *Physics*, *122*(2), 2655–2673. doi: 10.1002/2016JA022571

782 Laundal, K., Cnossen, I., Milan, S. E., Haaland, S. E., Coxon, J., Pedatella, N. M.,
783 ... Reistad, J. P. (2017). North-South asymmetries in Earth's magnetic field -
784 Effects on high-latitude geospace. *Space Sci. Reviews.*, *193*.

785 Laundal, K. M., & Richmond, A. D. (2016). Magnetic Coordinate Systems. *Space*
786 *Science Reviews*, 1–33. doi: 10.1007/s11214-016-0275-y

787 Lei, J., Wang, W., Burns, A. G., Luan, X., & Dou, X. (2016, jul). Can atomic
788 oxygen production explain the ionospheric annual asymmetry? *Jour-*
789 *nal of Geophysical Research: Space Physics*, *121*(7), 7238–7244. doi:
790 10.1002/2016JA022648

791 Li, K., Förster, M., Rong, Z., Haaland, S., Kronberg, E., Cui, J., ... Wei, Y. (2020,
792 mar). The Polar Wind Modulated by the Spatial Inhomogeneity of the
793 Strength of the Earth's Magnetic Field. *Journal of Geophysical Research:*
794 *Space Physics*, e2020JA027802. doi: 10.1029/2020JA027802

795 Li, K., Haaland, S., Eriksson, A., André, M., Engwall, E., Wei, Y., ... Ren, Q. Y.
796 (2012, Sep). On the ionospheric source region of cold ion outflow. *Geophysical*
797 *Research Letters*, *39*(18), L18102. doi: 10.1029/2012GL053297

798 Liu, C., Perez, J. D., Moore, T. E., & Chappell, C. R. (1994, feb). Low energy par-
799 ticle signature of substorm dipolarization. *Geophysical Research Letters*, *21*(3),
800 229–232. doi: 10.1029/93GL02839

801 Liu, L., & Chen, Y. (2009, oct). Statistical analysis of solar activity variations of
802 total electron content derived at Jet Propulsion Laboratory from GPS ob-
803 servations. *Journal of Geophysical Research: Space Physics*, *114*(A10). doi:

804 10.1029/2009JA014533

805 Lomidze, L., Knudsen, D. J., Burchill, J., Kouznetsov, A., & Buchert, S. C. (2018).
806 Calibration and validation of Swarm plasma densities and electron tempera-
807 tures using ground-based radars and satellite radio occultation measurements.
808 *Radio Science*, *53*(1), 15–36. doi: 10.1002/2017RS006415

809 Maes, L., Maggiolo, R., & De Keyser, J. (2016). Seasonal variations and north-south
810 asymmetries in polar wind outflow due to solar illumination. *Ann. Geophys.*,
811 *34*, 961-974. doi: doi:10.5194/angeo-34-961-2016

812 McNamara, L. F., Cooke, D. L., Valladares, C. E., & Reinisch, B. W. (2007, apr).
813 Comparison of CHAMP and Digisonde plasma frequencies at Jicamarca, Peru.
814 *Radio Science*, *42*(2). doi: 10.1029/2006RS003491

815 Mendillo, M., Huang, C.-L., Pi, X., Rishbeth, H., & Meier, R. (2005, oct).
816 The global ionospheric asymmetry in total electron content. *Journal*
817 *of Atmospheric and Solar-Terrestrial Physics*, *67*(15), 1377–1387. doi:
818 10.1016/j.jastp.2005.06.021

819 Mikhailov, A. V., & Schlegel, K. (2001). Equinoctial transitions in the ionosphere
820 and thermosphere. *Annales Geophysicæ*, *19*, 783-796. doi: 10.5194/angeo-19
821 -783-2001

822 Milan, S. E. (2009, Sep). Both solar wind-magnetosphere coupling and ring current
823 intensity control of the size of the auroral oval. *Geophysical Research Letters*,
824 *36*(18), L18101. doi: 10.1029/2009GL039997

825 Milan, S. E., Boakes, P. D., & Hubert, B. (2008, Sep). Response of the expand-
826 ing/contracting polar cap to weak and strong solar wind driving: Implications
827 for substorm onset. *Journal of Geophysical Research (Space Physics)*, *113*(A9),
828 A09215. doi: 10.1029/2008JA013340

829 Nilsson, H., Engwall, E., Eriksson, A., Puhl-Quinn, P. A., & Arvelius, S. (2010,
830 February). Centrifugal acceleration in the magnetotail lobes. *Annales Geophys-*
831 *icae*, *28*, 569-576. doi: 10.5194/angeo-28-569-2010

832 Nilsson, H., Waara, M., Marghitu, O., Yamauchi, M., Lundin, R., Rème, H., ...
833 Korth, A. (2008, February). An assessment of the role of the centrifugal ac-
834 celeration mechanism in high altitude polar cap oxygen ion outflow. *Annales*
835 *Geophysicae*, *26*, 145-157. doi: 10.5194/angeo-26-145-2008

836 Nishida, A. (1966, dec). Formation of plasmapause, or magnetospheric plasma

knee, by the combined action of magnetospheric convection and plasma escape from the tail. *Journal of Geophysical Research*, *71*(23), 5669–5679. doi: 10.1029/JZ071i023p05669

Pedregosa, F., Varoquaux, G., Gramfort, A., Michel, V., Thirion, B., Grisel, O., ... Duchesnay, E. (2011). Scikit-learn: Machine learning in Python. *Journal of Machine Learning Research*, *12*, 2825–2830.

Quinn, T. P., & Nisbet, J. S. (1965, Jan). Recombination and Transport in the Nighttime F Layer of the Ionosphere. *Journal of Geophysical Research: Space Physics*, *70*(1), 113-130. doi: 10.1029/JZ070i001p00113

Rees, M. H. (1963, Oct). Auroral ionization and excitation by incident energetic electrons. *Planetary and Space Science*, *11*(10), 1209-1218. doi: 10.1016/0032-0633(63)90252-6

Rees, M. H. (1982, May). On the interaction of auroral protons with the earth's atmosphere. *Planetary and Space Science*, *30*(5), 463-472. doi: 10.1016/0032-0633(82)90056-3

Rees, M. H. (1989). *Physics and chemistry of the upper atmosphere.* Cambridge, United Kingdom: Cambridge University Press.

Reigber, C., Lühr, H., Grunwaldt, L., Förste, C., König, R., Massmann, H., & Falck, C. (2006). CHAMP Mission 5 Years in Orbit. In *Observation of the earth system from space* (pp. 3–15). Berlin/Heidelberg: Springer-Verlag. doi: 10.1007/3-540-29522-4_1

Rhodes, B. (2019, Jul). *Skyfield: High precision research-grade positions for planets and Earth satellites generator.*

Richmond, A. D. (1995). Ionospheric Electrodynamics Using Magnetic Apex Coordinates. *Journal of geomagnetism and geoelectricity*, *47*(2), 191–212. doi: 10.5636/jgg.47.191

Rishbeth, H. (1962, Apr). Atmospheric composition and the F layer of the ionosphere. *Planetary and Space Science*, *9*(4), 149-152. doi: 10.1016/0032-0633(62)90002-8

Rishbeth, H. (1997, Oct). The ionospheric E-layer and F-layer dynamos - a tutorial review. *Journal of Atmospheric and Solar-Terrestrial Physics*, *59*, 1873-1880. doi: 10.1016/S1364-6826(97)00005-9

Rishbeth, H., & Müller-Wodarg, I. C. F. (2006, dec). Why is there more ionosphere

in January than in July? The annual asymmetry in the F2-layer. *Annales Geophysicae*, *24*(12), 3293–3311. doi: 10.5194/angeo-24-3293-2006

Rother, M., Choi, S., Mai, W., Lühr, H., & Cooke, D. (2005, jan). Status of the CHAMP ME data processing. In *Earth observation with champ results from three years in orbit* (p. 413). doi: 10.1007/3-540-26800-6_66

Schunk, R., & Nagy, A. (2009). *Ionospheres* (Second ed.). Cambridge: Cambridge University Press. doi: 10.1017/CBO9780511635342

Shim, J. S., Kuznetsova, M., Rastätter, L., Hesse, M., Bilitza, D., Butala, M., ... Rideout, B. (2011, dec). CEDAR Electrodynamics Thermosphere Ionosphere (ETI) Challenge for systematic assessment of ionosphere/thermosphere models: NmF2, hmF2, and vertical drift using ground-based observations. *Space Weather*, *9*(12). doi: 10.1029/2011SW000727

Sotirelis, T., Newell, P. T., & Meng, C. (1998, January). Shape of the open-closed boundary of the polar cap as determined from observations of precipitating particles by up to four DMSP satellites. *Journal of Geophysical Research: Space Physics*, *103*, 399-406. doi: 10.1029/97JA02437

Stankov, S., & Jakowski, N. (2006, jan). Topside ionospheric scale height analysis and modelling based on radio occultation measurements. *Journal of Atmospheric and Solar-Terrestrial Physics*, *68*(2), 134–162. doi: 10.1016/j.jastp.2005.10.003

Torr, D. G., Torr, M. R., & Richards, P. G. (1980, may). Causes of the F region winter anomaly. *Geophysical Research Letters*, *7*(5), 301–304. doi: 10.1029/GL007i005p00301

van der Meeren, C., Burrell, A. G., & Laundal, K. M. (2018). *apexpy: Apexpy version 1.0.3.* `http://doi.org/10.5281/zenodo.1214207`.

Velinov, P. (1970, Feb). Solar cosmic ray ionization in the low ionosphere. *Journal of Atmospheric and Terrestrial Physics*, *32*, 139-147. doi: 10.1016/0021-9169(70)90187-X

Virtanen, P., Gommers, R., Oliphant, T. E., Haberland, M., Reddy, T., Cournapeau, D., ... Contributors, S. . . (2020). SciPy 1.0: Fundamental Algorithms for Scientific Computing in Python. *Nature Methods*. doi: https://doi.org/10.1038/s41592-019-0686-2

Xiong, C., Stolle, C., & Park, J. (2018, apr). Climatology of GPS signal loss ob-

served by Swarm satellites. *Ann. Geophys.*, *36*(2), 679–693. doi: 10.5194/angeo
-36-679-2018